ACS OMEGA

Open Access

http://pubs.acs.org/journal/acsodf

Article

Fabrication of 2D Vanadium MXene Polyphenylsulfone Ultrafiltration Membrane for Enhancing the Water Flux and for Effective Separation of Humic Acid and Dyes from Wastewater

Prabhakar Satishkumar, Arun M. Isloor,* Lakshmi Nidhi Rao, and Ramin Farnood

Cite This: *ACS Omega* 2024, 9, 25766−25778

Read Online

ACCESS | Metrics & More | Article Recommendations | Supporting Information

ABSTRACT: MXene, a new 2D transition metal carbide-based material, is gaining outstanding attention in recent days in the area of separation and purification. In this study, we have successfully synthesized vanadium-based MXene-V_2CT_x (where T represents functional groups such as −OH, O, and F) by etching an aluminum layer from V_2AlC. For the first time, a vanadium-based MXene-V_2CT_x-embedded mixed matrix membrane was fabricated and utilized for removal of hazardous dye and humic acid from wastewater. With an increase in V_2CT_x loading, the hydrophilicity of the polyphenylsulfone (PPSU) membrane reasonably improved, and its water contact angle was reduced from 82.8 to 70.9°. V_2CT_x nanosheet-embedded PPSU membrane exhibited an excellent pure water permeability of 247 L m^{-2} h^{-1}, which was 266% elevated than the pristine PPSU membrane. The V_2CT_x-PPSU membrane revealed a good antifouling nature, thermal stability, and 98.5% removal of humic acid. The optimal membrane exhibited 96.6 and 82.02% expulsion of Reactive Black 5 (RB 5) dye and Reactive Orange 16 (RO 16) dye, respectively. The flux for RO 16 and RB 5 dyes and humic acid were remarkable with a value of 202.02, 161.61, and 141.41 L m^{-2} h^{-1}, respectively. This work provides a new V_2CT_x-incorporated PPSU ultrafiltration membrane to effectively treat humic acid and dye wastewater.

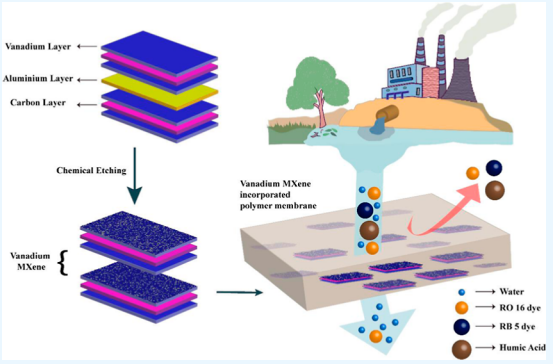

1. INTRODUCTION

At present, one of the potential threats to humanity is the acute shortage of potable water and the intensification of water pollution. The overgrowing population and swift increase in the growth of industries to meet the demands of humanity account for the pollution of water.[1] Over and above 700,000 tons of dyes were manufactured annually by industries involving plastic, food, cosmetics, textiles, and paper.[2] A portion of prepared dyes find their way to water bodies through industrial effluents. The majority of the dyes do not degrade and cause various health complications like cancer, liver malfunction, allergies, and skin diseases.[3] It also affects the aquatic life forms by lowering the dissolved oxygen, causing eutrophication and disturbing the ecosystem.[4] Humic acid (HA) is a natural organic matter that exists in water sources due to the decomposition of animal and plant materials in the environment. When it comes in contact with chlorine during the disinfection process, it produces highly carcinogenic products such as trihalomethanes and haloacetic acids.[5] HA also reduces the removal efficiency of dyes and heavy metals by making complexes with them. Thus, the elimination of HA and dyes from polluted water is of paramount importance for water purification.

Membrane technology involving ultrafiltration (UF) provides a less energy-demanding and high separation efficiency pathway to remove dyes and HA from polluted water sources. Polymeric membranes are abundantly used for purification due to their ease of processability and chemical stability. Polyphenylsulfone (PPSU) is an excellent sulfonated polymer that exhibits good mechanical strength, high resistance to hydrolysis, thermal stability at high temperatures, and a vast array of chemical compatibility.[6] However, the hydrophobic nature of PPSU facilitates the adhesion of contaminants such as HA on the membrane surface, leading to fouling by blocking its pores. To overcome fouling, hydrophilic inorganic additives are added to polymeric membranes. The addition of inorganic additives can significantly alter the features of the polymeric membranes in the matter of antifouling nature, water uptake, mechanical stability, thermal stability, and superior permeability.[7,8]

Plenty of polymeric heterogeneous mixed matrix membranes (MMMs) were fabricated with inorganic additives such as TiO_2,[9] calcium carbonate,[10] tin oxide,[11] ferric oxide,[12]

Received: December 17, 2023
Revised: March 12, 2024
Accepted: March 15, 2024
Published: June 3, 2024

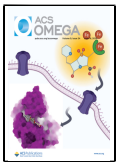

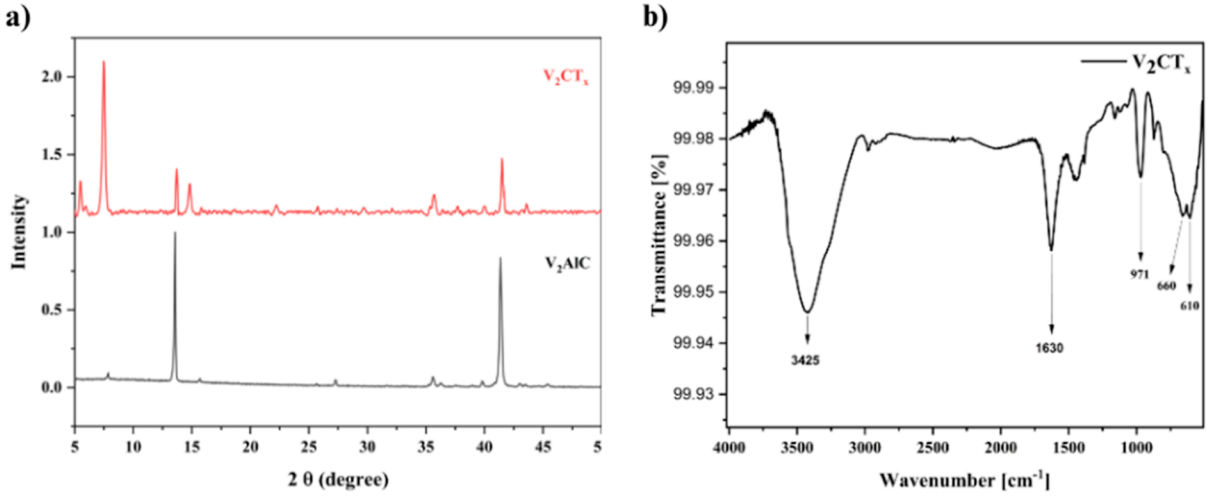

Figure 1. (a) XRD spectra of V_2CT_x MXene and the V_2AlC MAX phase. (b) FTIR spectra of V_2CT_x MXene.

aluminum oxide,[13] graphene,[14] and many more. Graphene oxide (GO) has gained more attention due to its distinctive 2D structure, and GO-embedded membranes were demonstrated to be promising membranes for liquid and gas separation. However, the permeability of GO membranes was relatively less due to the small interlayer spacing.[15] Generally, 2D materials exhibit sheet-like structures with atomic thickness, properly stacked 2D transport channels, and micrometer lateral size.[16] Thus, they are effectively utilized in membranes for various high-performance separation applications.

Nowadays, a new family of 2D materials named 'MXene' is gaining remarkable attention due to its excellent hydrophilic surface, good chemical strength, structural stability, and tunable interlayer spacing. MXene materials are 2D transition metal carbide, nitride, or carbonitrides, with a common formula of $M_{n+1}X_n$ or $M_{n+1}X_nT_x$ in which M designates early transition metals (e.g., V, Nb, Sc, Cr, and Ti), X stands for carbon and/or nitrogen, and T denotes surface functionalities such as −OH, −O, or −F. $Ti_3C_2T_x$ was the first MXene synthesized by Naguib and group members in 2011.[17] However, reports of MXene-incorporated membranes were obtained in 2017. MXenes found expansive utilization in the areas of energy storage,[18] sensing,[19] catalysis,[20] membranes,[21] and biomedicine.[22] Among all, only 6% of MXene-related literature are in association with membranes and purification.[23] Ding and group members deposited $Ti_3C_2T_x$ on porous anodic aluminum oxide (AAO) support and with the aid of $Fe(OH)_3$ colloidal solution.[24] The as-prepared $Ti_3C_2T_x$/AAO membranes showed 90% rejection of Evans blue and 90% removal of rhodamine B dye. $Ti_3C_2T_x$ surface-deposited polyether sulfone (PES) composite membrane prepared by Han and coworkers exhibited 80.3% removal of gentian violet and 92.3% removal of Congo red dye.[15] It also showed a notable pure water flux (PWF) of 115 L m^{-2} h^{-1} at 0.1 MPa. Lin and group members mixed polydopamine (PDA) with $Ti_3C_2T_x$ MXene and by using vacuum-assisted filtration deposited it on cellulose acetate support.[25] $Ti_3C_2T_x$-PDA-CA membrane displayed 88.6% removal of direct black 38 and 88.9% removal of direct red dyes.

The majority of the MXene-incorporated membranes were fabricated by vacuum-assisted filtration, and MMMs were rarely available in the literature.[26−29] Dashtbozorg and group members reported polysulfone MMMs with $Ti_3C_2T_x$, and it showed more than 90% rejection of methyl orange.[30] However, the PWF of the membrane was found to be less than 48 L m^{-2} h^{-1}. Even though various other transition metal MXene compositions are available, the MXenes used for membranes are all of titanium (predominantly $Ti_3C_2T_x$) mainly due to its established synthetic route. Compared to other MXenes, the M_2XT_x composition, specifically V_2CT_x is entrancing due to its larger active area per mass and presence of more active transition metal.[31] V_2CT_x Mxene have been utilized in areas of supercapacitors,[32] optics,[33] batteries,[34] gas sensors,[35] and in nuclear waste treatment as a uranium capture material.[36] To the best of our knowledge, vanadium-based MXenes have not been utilized for membrane fabrication so far. This work involved the synthesis of vanadium MXene-V_2CT_x from its MAX phase (V_2AlC) using hydrogen fluoride and its incorporation into a PPSU polymer to fabricate an MMM for the first time. The successful synthesis of V_2CT_x particles was confirmed by analyzing their morphologies, elemental compositions, and X-ray diffraction (XRD) data. V_2CT_x particle size, zeta potential, and surface area analyses were also determined. The prepared V_2CT_x-PPSU MMMs with different V_2CT_x concentrations were systematically studied in relation to their hydrophilicity, temperature stability, PWF, separation performance, and antifouling nature.

2. RESULTS AND DISCUSSION

2.1. Characterization of V_2CT_x MXene Nanosheets. The successful synthesis of V_2CT_x MXene nanosheets from V_2AlC was confirmed by powder XRD analysis. XRD patterns of both synthesized V_2CT_x MXene nanosheets and V_2AlC are shown in Figure 1a. The characteristic diffraction peak with 2θ values at 7.5° belongs to the (002) plane of V_2CT_x MXene, consistent with the previous results.[37,38] A small amount of unetched V_2AlC presence was noticed by the diffraction peaks with 2θ values at 13.72 and 41.50°, which corresponds to (002) and (103) crystal planes.[39] The shift in the diffraction peak from 13.72° to a lower angle of 7.5° in the V_2CT_x was due to the enlargement of interlayer spacing by the removal of the Al layer from V_2AlC. The chemical bonding interaction of the synthesized V_2CT_x MXene nanosheets was done by attenuated total reflectance Fourier transform infrared (ATR-FTIR) spectroscopy and is represented in Figure 1b. The peaks observed at 3425 and 1630 cm^{-1} are due to the strongly

https://doi.org/10.1021/acsomega.3c10078
ACS Omega 2024, 9, 25766−25778

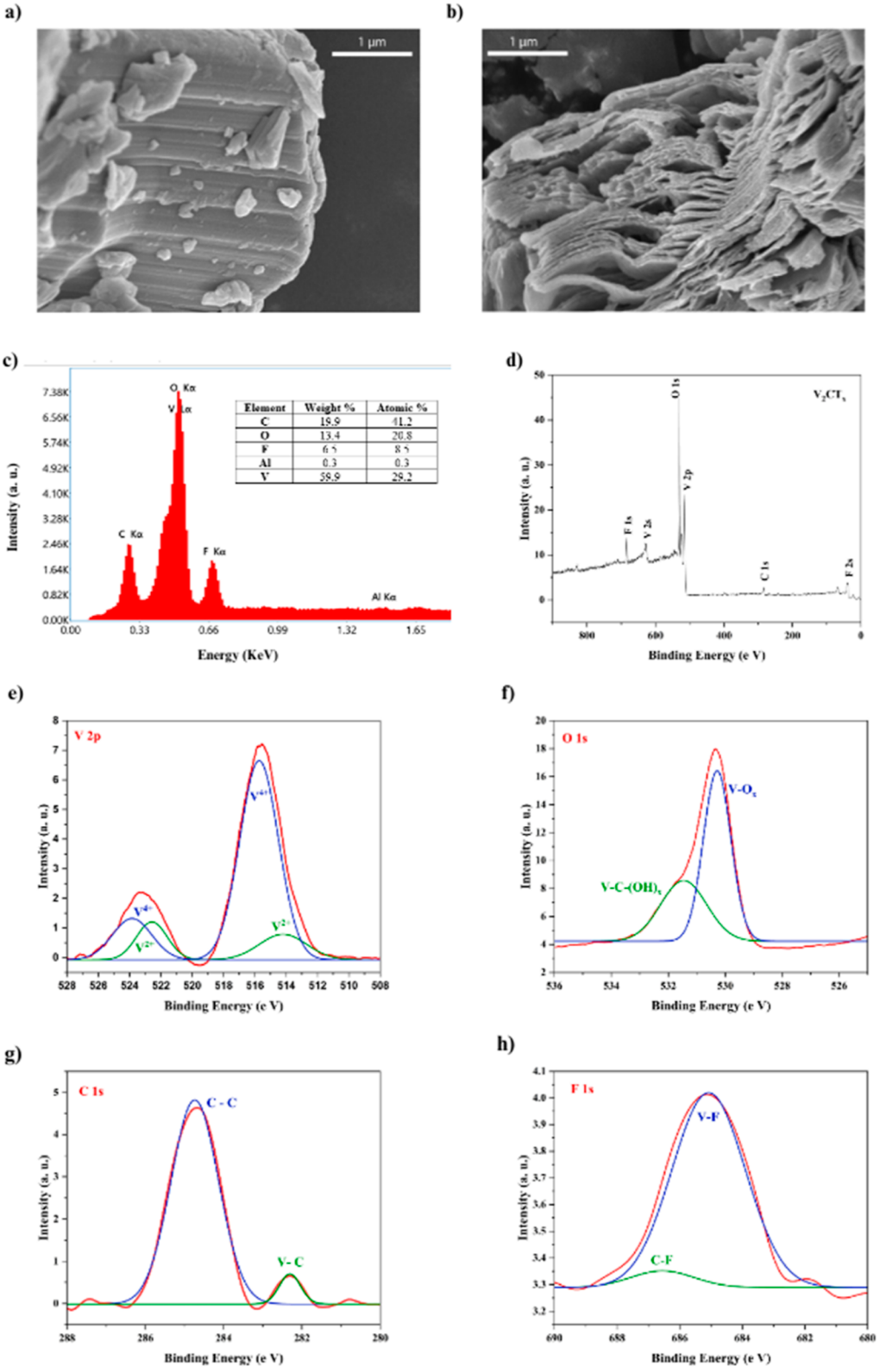

Figure 2. FESEM images of (a) V_2AlC and (b) V_2CT_x particles. V_2CT_x (c) EDAX spectra and (d−h) XPS spectra.

adsorbed hydrogen-bonded external water molecules to the −OH groups present on the surface of V_2CT_x MXene nanosheets.[40] Peaks at 971 and 660 cm^{-1} correspond to V═O and V−OH vibrations, respectively.[41,42] V−C stretching vibration was perceived at 610 cm^{-1}.

The scanning electron microscopy (SEM) images of the vanadium MAX phase (V_2AlC) and obtained vanadium MXene (V_2CT_x) are shown in Figure 2a,b, respectively. V_2AlC particles displayed a dense ceramic structure before etching. V_2CT_x particles revealed an accordion-like structure, which is a typical multilayered structure exhibited by

https://doi.org/10.1021/acsomega.3c10078
ACS Omega 2024, 9, 25766−25778

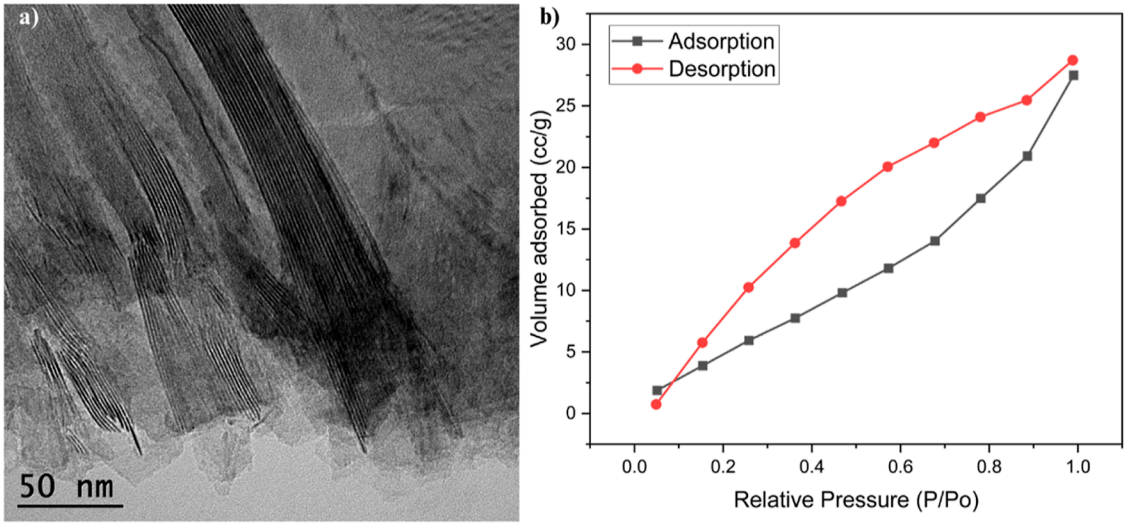

Figure 3. (a) TEM image of V_2CT_x MXene nanosheets. (b) BET isotherm plot for nitrogen adsorption and desorption on V_2CT_x MXene nanosheets.

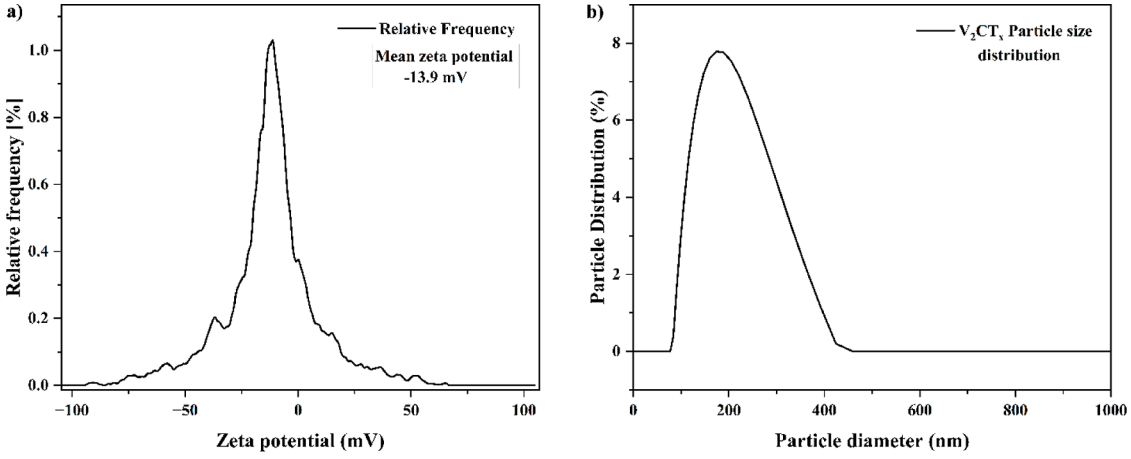

Figure 4. (a) Zeta potential and (b) particle size distribution of V_2CT_x particles.

MXenes.[43] SEM images apparently showed the successful etching of the Al layer from V_2AlC particles, and it was further confirmed by energy dispersive X-ray spectroscopy (EDX) analysis. Figure 2c shows the EDX analysis of V_2CT_x particles. The atomic % of V, C, O, F, and Al were found to be 28.9, 42.2, 19.0, 9.3 and 0.6, respectively, after hydrogen fluoride (HF) treatment. The very high concentration of C is due to the carbon tapes since the EDX tests were done on powders scattered on carbon tapes. However, to get mean atomic concentrations, we cannot focus a powder to high-magnification EDX tests. Even though the purity of the synthesized V_2CT_x can be evaluated from the V/Al ratio of samples, the atomic ratio of V/C/O/F/Al was detected to be 1:1.4:0.6:0.3:0.02, respectively, which agrees with the previous reports.[37] The obtained Al atomic ratio is only 2.07%, in comparison with vanadium. It suggests the efficient synthesis of pure V_2CT_x with negligible unetched V_2AlC. EDX analysis also revealed the presence of O and F terminations on the surface. X-ray photoelectron spectroscopy (XPS) analysis of V_2CT_x was done and the results are plotted in Figure 2d–h. XPS study confirmed the presence of V, O, F and C elements and is shown in Figure 2d. A high-resolution spectrum of V 2p is given in Figure 2e which shows the presence of vanadium predominantly in the V^{4+} oxidation state at a binding energy of 515.76 and 523.8 eV, in well accordance with previous reports in the literature.[34,39] The high oxidation state of vanadium is attributed to oxygen-containing surface groups on the surface of V_2CT_x MXene layers. The V 2p curve was best fitted with a small amount of V^{2+} elements present at 513.9 and 522.5 eV. Figure 2f depicts the deconvolution of the XPS spectrum for O 1s region. An intense peak at 530.6 eV is ascribed to the oxygen functional group attached to vanadium. Another peak at 531.8 eV corresponds to $V-C-(OH)_x$ bonds which agree with reported values in the literature.[35,44] C 1s XPS region and its deconvolution are displayed in Figure 2g. The V–C and C–C bonding interactions are represented by binding energy values of 282.31 and 284.74 eV, respectively. Figure 2h reveals the presence of fluorine terminations on the V_2CT_x MXene surface by the appearance of a peak at 684.86 eV.

A high-resolution transmission electron microscopy (TEM) image of V_2CT_x MXene nanosheets is provided in Figure 3a, and it clearly manifests the stacked multilayered structure. V_2CT_x MXene nanosheets exhibited a typical 2D structure with a large area and a small thickness of a few nanometers. The Brunauer–Emmett–Teller (BET) adsorption study further confirmed the pore structure. The BET analysis of

https://doi.org/10.1021/acsomega.3c10078
ACS Omega 2024, 9, 25766–25778

V_2CT_x particles is presented in Figure 3b, and it involved N_2 gas adsorption and desorption studies. From the results, it is evident that it belongs to a type IV isotherm accompanied by an H3 hysteresis loop, which suggests multilayer adsorption with capillary condensation. Conforming to the International Union of Pure and Applied Chemistry classifications, the H3 hysteresis loop specifies groove pores formed by flaky particles with mesoporous and microporous features.[6,45] The surface area and pore volume of the V_2CT_x MXene nanosheets were found to be 26.699 m^2 g^{-1} from multipoint BET plot and 0.035 cc g^{-1} from BJH desorption, respectively.

The superficial charge of V_2AlC and synthesized V_2CT_x MXene nanosheets was determined by a zeta potential study and is given in Figure 4a,b, respectively. The electrical potential measured at the interface of the electrical double layer attached to the particle surface and the free-moving mobile fluid was termed zeta potential. As the zeta potential of the particle increases its possibility of agglomeration decreases due to the electrostatic repulsion. V_2AlC and V_2CT_x particles displayed zeta potentials of −5.8 and −13.9 mV, respectively. The zeta potential of V_2CT_x particles significantly increased, attributable to the attachment of hydroxyl groups on its surface, and it also indicates rich polar functional groups on the surface. The higher zeta potential of V_2CT_x particles inhibits its agglomeration and facilitates stable dispersion by increasing colloidal stability.[46] The particle size distribution of V_2CT_x is shown in Figure 4b. The hydrodynamic diameter of V_2CT_x MXene nanosheets was found to be 224.8 nm.

2.2. Membrane Characterization. The cross-sectional FESEM images of all the fabricated membranes are provided in Figure 5a−d. Each of the membranes revealed an unsymmetrical structure with macro voids in the sublayer and finger-like microvoids in the upper layer which is the classic appearance of UF membranes.[47] The pristine PPSU membrane's microporous structure was not uniform and lacked proper finger-like projections. Adding PVP within the dope solution speeds up the phase inversion process, enlarges the macro voids, and acts as a pore-creating factor. The incorporation of hydrophilic V_2CT_x MXene nanosheets enhanced the speed of demixing betwixt the nonsolvent and solvent, which successively produced a more porous membrane. Vertical finger-like microvoids were more prominent in V_2CT_x nanosheet-embedded membranes, facilitating the quick movement of water flow with less in-house resistance. VPM-2 membranes exhibited large macro voids and unhindered long microvoids compared to VPM-1 and VPM-3 membranes, accounting for their better performance.

The effect of synthesized V_2CT_x nanosheets on the contact angle, water uptake, and porosity of the prepared membranes is given in Table 1. The contact angle quantifies the water affinity of the active surface of the prepared membranes. Hydrophilicity significantly improves the membrane performance in terms of flux, rejection, and antifouling nature.[48] Lower contact angle values indicate the inflated relationship of water molecules with regard to the membranes. The neat PPSU membrane displayed a water contact angle of 82.8°. An increment in the dosage of hydrophilic V_2CT_x nanosheets from 0.5 to 1.5 wt % notably decreased the water contact angle from 77° for VPM-1 to 70.9° for VPM-3 (Figure 6).

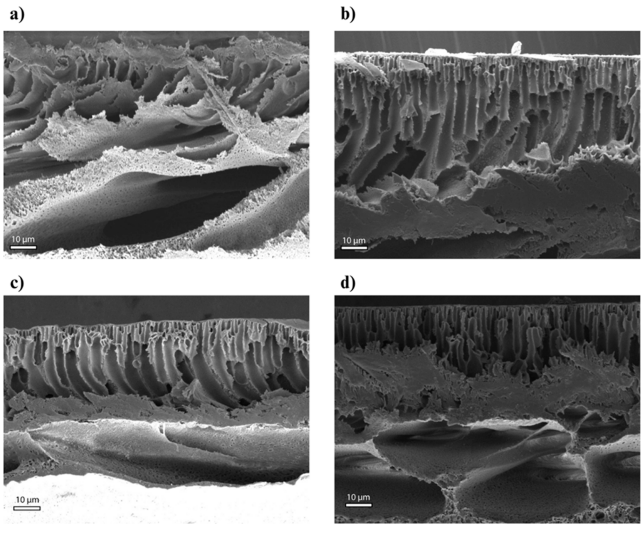

Figure 5. Cross-sectional FESEM images of the membrane: (a) VPM-0, (b) VPM-1, (c) VPM-2, and (d) VPM-3.

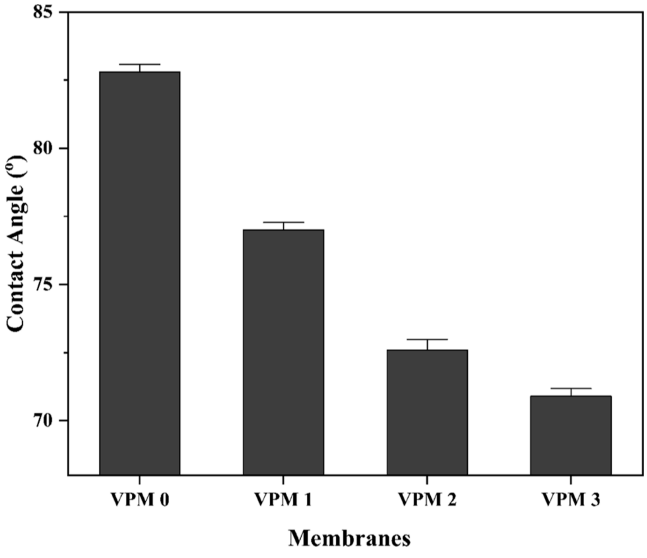

Figure 6. Water contact angle of membranes.

The remarkable decline in the water contact angle is attributed to the polar hydroxyl groups existing on the V_2CT_x nanosheets, which modify the membrane boundary free energy. VPM-2 showed the highest water uptake of 74.21%,

Table 1. Membrane Water Contact Angle, Water Uptake, Porosity, and Surface Roughness Parameters

membrane	water contact angle (deg)	water uptake (%)	porosity (%)	RMS roughness (SR_q)	average roughness (SR_a)
VPM-0	82.8 ± 0.3	34.63 ± 0.2	30.06 ± 0.3	5.41	3.26
VPM-1	77.0 ± 0.2	45.38 ± 0.9	52.04 ± 0.5	7.00	5.21
VPM-2	72.6 ± 0.4	62.29 ± 0.6	75.44 ± 0.7	8.42	5.71
VPM-3	70.9 ± 0.3	56.68 ± 0.5	63.15 ± 0.8	6.39	4.77

https://doi.org/10.1021/acsomega.3c10078
ACS Omega 2024, 9, 25766−25778

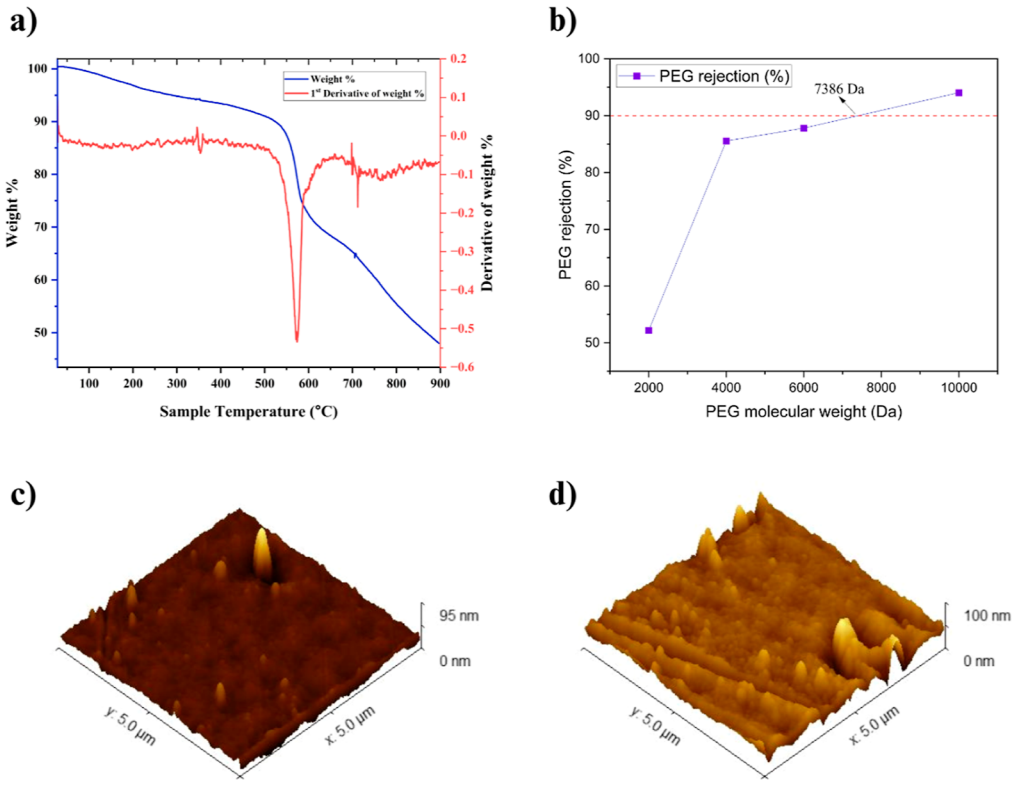

Figure 7. (a) TGA of VPM-2 membrane. (b) MWCO plot of VPM-2 membrane. AFM images of membranes of (c) VPM-0 and (d) VPM-2.

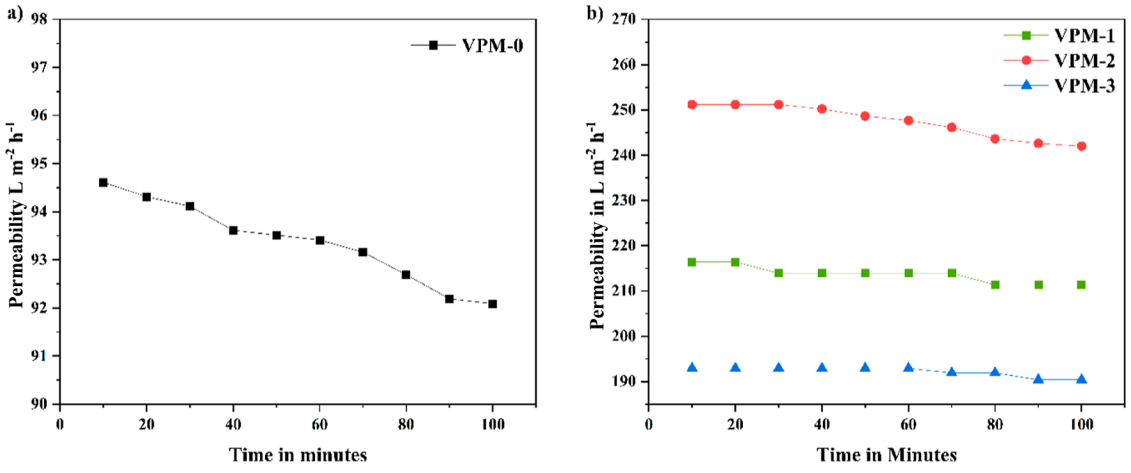

Figure 8. Pure water permeability of the (a) VPM-0 and (b) VPM-1, VPM-2, and VPM-3 membranes at a 2 bar pressure.

while VPM-0 showed only 49.02% water uptake strength. Even though VPM-3 exhibited the highest hydrophilicity among the prepared membranes, its water uptake strength was less than VPM-2. At a higher concentration, the partial agglomeration of the nanosheets increases the viscosity of the dope solution which in turn reduces the demixing process in phase inversion.[49,50] It results in reduced porosity and water uptake. Porosity calculations also support the superior porous structure of VPM-2 compared to all of the other fabricated membranes, with a value of 85.44%. The enhanced water uptake strength could be ascribed to increased porosity, resulting in increased void for capillary adsorbed water.[51]

The thermal stability of the fabricated VPM-2 membrane was analyzed using a thermogravimetric analysis (TGA) and is shown in Figure 7a. The small amount of weight loss detected from 60° to 150 °C corresponds to adsorbed water. The predominant weight loss was noticed in the sweep of 500° to 600 °C, which stipulates the degradation temperature of the membrane. From TGA analysis, it is noticeable that the VPM-2 membrane can sustain up to 550 °C and possesses good thermal stability.

The VPM-2 membrane molecular weight cutoff (MWCO) was studied by using different molecular weight PEG solutions. With an increase in the molecular weight of PEG solutions, its rejection percentage also increased correspondingly as represented in Figure 7b. MWCO of the VPM-2 membrane was determined to be 7386 Da, validating that the fabricated membrane is an UF membrane.

The surface topography and roughness parameters of the fabricated membranes were scrutinized by using atomic force

https://doi.org/10.1021/acsomega.3c10078
ACS Omega 2024, 9, 25766−25778

microscopy (AFM). Figure 7c,d depicts the 3D surface (5 × 5 μm) of the pristine PPSU and VPM-2 membranes, respectively. The surface roughness parameters, such as root mean square (RMS) roughness (SRq) and mean roughness (SRa) of all the fabricated membranes, are mentioned in Table 1. With an augmentation in V_2CT_x nanosheets loading from 0 to 1 wt %, the surface roughness of the membranes increased, and it was ascribed to the hydrophilic nature of V_2CT_x nanosheets. During the demixing process, the hydrophilic V_2CT_x nanosheets migrate to the aqueous phase interface, resulting in a rough surface topography.[52] However, the surface roughness of VPM-3 was less compared to that of VPM-2 due to the partial agglomeration of nanosheets at higher concentrations. The increment in surface roughness enhances the surface area and active sites on the membrane, eventually leading to higher flux.

2.3. Filtration Performance. The PWF of the fabricated membrane was tested by making use of a cross-flow filtration equipment at a pressure of 2 bar, and the obtained results are plotted in Figure 8. The VPM-2 membrane displayed an excellent PWF of 247.39 L m^{-2} $h^{-1,}$ while the VPM-0 membrane provided only 93.4 L m^{-2} h^{-1}. Incorporation of V_2CT_x nanosheets augmented the membrane PWF to 264% compared with the neat membrane. Pronounced hydrophilicity and rich polar functional groups on the embedded V_2CT_x nanosheets greatly facilitate water movement through the membrane. The highest PWP shown by the VPM-2 membrane can be ascribed to its better porosity compared to other membranes. VPM-2 showed higher pure water permeability than VPM-3 due to the two main reasons. First, the presence of large macro voids in the sublayer is significant compared to VPM-3. Second, a rougher surface of VPM-2 resulted in higher active sites and additional surface area for filtration.

2.4. Antifouling Analysis. The filtration performance of the prepared membrane on lengthy usage was studied using its antifouling properties, and the obtained flux is tabulated in Table 2. When the membranes are exposed to long-term usage, the foulants gradually tend to accumulate on the membrane surface and reduce their filtration ability by plugging the pores.

Table 2. Membrane Filtration Performance at a 2 bar Pressure

membrane	pure water flux (J_{f_1}) (L m^{-2} h^{-1})	BSA flux (J_b) (L m^{-2} h^{-1})	water flux after the wash (J_{f_2}) (L m^{-2} h^{-1})
VPM-0	93.40 ± 1.21	53.01 ± 0.20	63.11 ± 1.30
VPM-1	214.57 ± 1.86	138.84 ± 3.10	146.41 ± 1.30
VPM-2	247.39 ± 3.80	164.08 ± 2.96	184.28 ± 1.21
VPM-3	191.85 ± 1.06	121.17 ± 1.30	131.26 ± 2.21

In this work, bovine serum albumin (BSA) was used as a model foulant, and an antifouling study of all of the prepared membranes is shown in Figure 9. From the plot, it is clear that with all the membranes the water flux diminished during BSA filtration which was due to the concentration polarization and deposition of large BSA protein molecules on the membrane surface.[53,54] However, the VPM-2 membrane displayed a better antifouling nature than the VPM-0 membrane in connection with the flux recovery ratio, irreversible fouling, and total fouling. It can be attributed to the rougher surface of VPM-2 in comparison with VPM-0. A smooth surface facilitates dense fouling layer formation, whereas a rough surface forms a loose fouling layer, resulting in lesser flow resistance [[29]. The

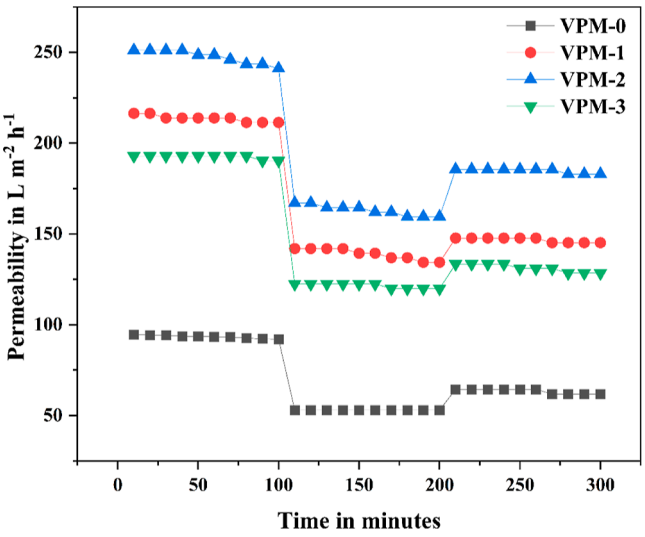

Figure 9. Flux of pure water, BSA solution, and water after washing with deionized water.

presence of V_2CT_x nanosheets was another reason for less foulant adsorption on the composite membrane surface. Hydrophilic V_2CT_x nanosheets on the membrane surface form an aqueous layer that lowers the interaction between protein molecules and the membrane.[55−57] The highest fux recovery ratio (FRR) of 75.26% was observed for the VPM-2 membranes, with the least value of 24.7% irreversible fouling.

2.5. Separation Study. Based on the PWP and FRR, VPM-2 membrane was opted for HA and dyes' separation study. The rejection percentage of the VPM-2 membrane with respect to HA, RB 5, and RO 16 is shown in Figure 10a along with the photographs of its feed and permeates in Figure 10b. VPM-2 membrane showed 98.5% removal of HA. The HA removal efficiency of the membrane was mainly due to its hydrophilicity and surface charge.[58] The enhanced water affinity of the VPM-2 membrane with the addition of V_2CT_x nanosheets creates a hydration covering of the active membrane exterior. Hydration layer lowers the interplay of HA with the membrane exterior and improves the rejection performance. HA is a negatively charged molecule since it possesses −COOH and −OH functional groups. The incorporation of V_2CT_x nanosheets builds up the negative charge on the membrane surface, ascribed to the existence of a rich polar hydroxyl group on it. The strong electrostatic repulsion between the membrane and HA molecule accounts for its improved HA rejection.[59]

The RB 5 dye removal efficiency reached up to 96.6% for VPM-2 membrane from 91.2% for the VPM-0 membrane. The notable improvement in the rejection was due to the electrostatic repulsion between the negatively charged V_2CT_x nanosheets present on the membrane surface and negatively charged sulfonate groups of RB 5 dye molecules. 82.02% rejection of RO 16 dye was observed with VPM-2 membrane, while VPM-0 removal efficiency reached only up to 76%. RO 16 dye also possesses sulfonate groups, leading to its negative charge. Thus, electrostatic repulsion plays a key role in RO 16 dye removal efficiency of VPM-2 membrane by preventing its adsorption on the membrane surface. Moreover, RB 5 dye rejection strength of VPM-2 membrane was found to be more compared to RO 16 dye rejection. It can be attributed to the size debarment mechanism.[60] The RB 5 dye molecule

https://doi.org/10.1021/acsomega.3c10078
ACS Omega 2024, 9, 25766−25778

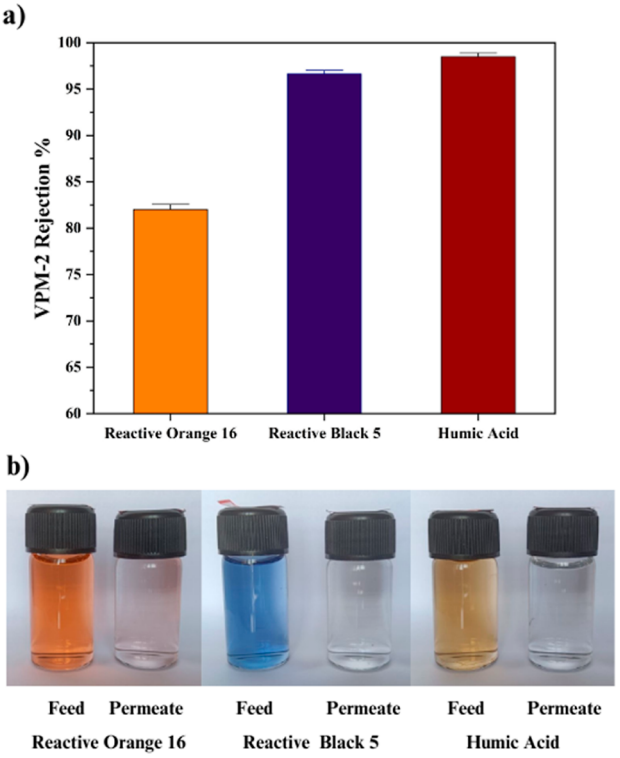

Figure 10. (a) Reactive Orange 16 dye, Reactive Black 5 dye, and HA rejection percentage of VPM-2 membrane and (b) photographs of their feed and permeate.

possesses a larger structure with high molecular weight compared to RO 16 dye, and it experiences more hindrance to passing through the narrow pores of the membrane.[61] The separation performance of V_2CT_x-PPSU membrane with other MXene-incorporated polymer membranes are compared in Table 3.

2.6. Membrane Reusability. The tendency of the membrane to be reused many times with approximately same efficiency is a very important factor to install and scale up the membrane in industrial wastewater application. V_2CT_x/PPSU composite membrane was tested for five cycles and its removal efficiency and flux were determined. After the first cycle, the composite membrane was rinsed with deionized (DI) water, and a back wash was given with DI water to use it for the next cycle. VPM-2 membrane showed negligible reduction in removal efficiency of HA and dyes and it is represented in Figure 11a. After five cycles, the VPM-2 membrane removal efficiency of HA, RO 16, and RB 5 was found to be 97.43, 95.24, and 81.1%, respectively. Figure 11b shows the variation of the flux after each cycle. A reasonably small decrement in flux was observed after five cycles and it was found to be 3.65, 3.99, and 4.79% for RO 16, RB 5, and HA, respectively.

3. CONCLUSIONS

Vanadium-based MXene-V_2CT_x was synthesized by the HF etching method and characterized by FESEM, EDX, TEM, FTIR, and BET. The particle size and zeta potential of the synthesized V_2CT_x MXene nanosheets were also determined. For the first time, a vanadium-based MXene-V_2CT_x-embedded MMM was fabricated. Incorporation of hydrophilic V_2CT_x MXene nanosheets significantly enhanced the hydrophilicity and porosity of the nanocomposite membrane. The contact angle decreased from 82.8° for VPM-0 to 70.9° for VPM-3, which can be ascribed to the rich polar functional groups present on the V_2CT_x MXene nanosheets. VPM-2 provided an outstanding PWP of 247.39 L m^{-2} $h^{-1,}$ which is 266% higher than that of the pristine PPSU membrane. It also showed an excellent thermal stability up to 500 °C. With an increase in V_2CT_x MXene nanosheet loading from 0 to 1 wt %, enhancement in the surface roughness, antifouling nature, and PWP of the nanocomposite membranes were observed. VPM-2 exhibited 98.5, 96.6, and 82.02% rejection of hazardous pollutants such as HAand RB 5 and RO 16 dyes, respectively. The exceptional PWP and notable pollutant removal efficiency of V_2CT_x MXene nanosheet-embedded PPSU nanocomposite membranes make them promising materials in UF and water purification.

4. METHODS AND MATERIALS

4.1. Chemicals. PPSU (Radel R-5000) was purchased from Solvay Specialty Polymers. 1-Methyl-2-pyrrolidone (NMP), polyvinylpyrrolidone (PVP-K30), and HF were procured from Loba Chemie. Vanadium aluminum carbide (V_2AlC) powder was purchased from Intelligent Materials Pvt. Ltd. BSA and HA were obtained from Himedia. Reactive Black 5 dye and Reactive Orange 16 dye were purchased from Sigma-Aldrich.

4.2. Synthesis of Vanadium MXene. The aluminum layer of the V_2AlC MAX phase was selectively etched using a 40% HF solution. Vanadium aluminum carbide powders (1g) were added to 20 mL of HF solution containing 10 mL of HCl in a Teflon jar and stirred for 84 h at 80 °C in an oil bath.

Table 3. Comparison of the V_2CT_x-PPSU Membrane with Other MXene-Incorporated Polymer Membranes Reported in the Literature

membrane	fabrication method	dyes/pollutant	rejection %	flux in L m−2 h−1 bar−1	refs
Ti3C2Tx/PES	vacuum filtration	Congo Red	92.3	115	15
		Gentian Violet	80.3	117	
Ti3C2Tx/PVDF	vacuum filtration	Rhodamine B	81.04	90.28	62
		Methyl Green	94.09	84.53	
Ti_3C_2Tx/PDA/RGO	vacuum filtration	Congo Red	95	174.16	63
Ti_3C_2Tx/ZIF-8/PES	MMM	Rhodamine B	98	170	64
Ti_3C_2Tx/PDA/CA	vacuum filtration	Direct Red	88.9	170	25
Ti_3C_2Tx/PEI	thin-film composite	Methyl Blue	98.84	20.9	65
V_2CTx/PPSU	MMM	Reactive orange 16	82.02	202.02	this work
		Reactive Black 5	96.6	161.61	
		humic acid	98.5	141.41	

https://doi.org/10.1021/acsomega.3c10078
ACS Omega 2024, 9, 25766−25778

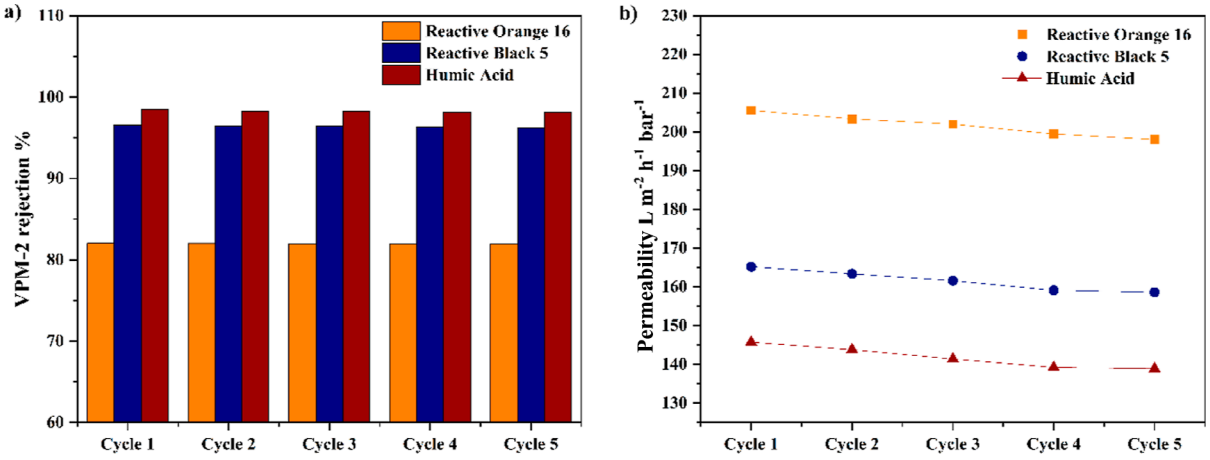

Figure 11. VPM-2 membrane (a) dyes' and HA rejection and (b) variation of flux for five cycles.

Later, the reaction mixture was repeatedly washed with DI water and centrifuged until the pH of the solution crossed above five as reported elsewhere.[66] The residue obtained was dried in a vacuum oven at 60 °C for 50 h to get V_2CT_x powder. In detail, a synthetic procedure is given in the Supporting Information.

4.3. Preparation of Vanadium MXene/PPSU Composite Membrane. The PPSU was dried at 50 °C in an oven to remove adsorbed moisture before usage. Four different membranes were fabricated via the immersion precipitation phase inversion method. The composition of casting solutions is presented in Table 4. The calculated quantity of V_2CT_x powders was dispersed in NMP using the probe sonicator in an ice-cold condition. 1 g of PVP was added to the dispersed solution as a pore-forming agent and stirred continuously for 24 h to attain a homogeneous solution. Afterward, the formed casting solution was degassed for 30 min to get rid of air bubbles. An automatic membrane casting instrument (K-202 control coater, purchased from UK) was used to cast the dope solution on a glass plate, and it was immersed inside a coagulation bath containing DI water as a nonsolvent. Phase inversion occurred in the coagulation bath, and the formed membrane was kept in DI water at normal temperature for 24 h with occasional interchange of DI water to take out the residual solvents. Further studies were done by washing the membranes with DI water.

Table 4. Membrane Compositions

membrane	PPSU (g)	NMP (g)	PVP (g)	V_2CT_x (g)	V_2CT_x (wt %)
VPM-0	20	79.0	1	0	0
VPM-1	20	78.9	1	0.1	0.5
VPM-2	20	78.8	1	0.2	1.0
VPM-3	20	78.7	1	0.3	1.5

4.4. Characterization of the Synthesized Vanadium MXene. Synthesized vanadium MXene (V_2CT_x) nanosheet structural morphology was examined by utilizing FESEM (7610FPLUS, Jeol). The elemental composition and atomic % of V_2CT_x were determined utilizing EDX (EDAX APEX). The functional groups and elemental bonding interactions present in V_2CT_x were studied by FTIR spectroscopy. The sample was studied in the range of 500−4000 cm^{-1}. For TEM analysis, V_2CT_x was dispersed in ethanol using a sonicator, and dispersed particles were placed on a 200 mesh size carbon-coated copper grid. V_2CT_x particles were analyzed using an FEI Tecnai G2 F30 S-Twin transmission electron microscope under a 300 kV acceleration voltage. V_2CT_x was dispersed in DI water and by employing zeta potential and particle size analyzer (3 Litesizer TM 500, Anton Paar) its size distribution and surface charge were determined. The surface area exhibited by V_2CT_x MXene nanosheets was determined by a BET surface area analyzer (Autosorb I-XR-XR, Anton Paar). The crystal structure of V_2CT_x was studied using powder XRD (Empyrean third generation, Malvern PANalytical) with a scan range (angles-2θ) from 4 to 60°.

4.5. Membrane Characterizations. *4.5.1. Membrane Morphology.* The prepared membranes were dipped in liquid nitrogen and fragmented to achieve sharp edges for analysis. Thus, the obtained membrane samples were coated with gold to circumvent charging. The cross-sectional portrayal of membranes was obtained by FESEM (7610FPLUS, JEOL). To study the incorporation and distribution of vanadium MXene in the fabricated membranes, those were subjected to EDX analysis at 10 kV. Surface roughness parameters of the membranes were investigated by AFM (Flex-Axiom Nanosurf). Dried membrane samples were used for this analysis. Surface roughness parameters like RMS roughness (SRq) and mean roughness (SRa) were obtained with Gwyddion software.

4.5.2. Contact Angle Measurements. Membrane hydrophilicity and surface wettability were measured in terms of the water contact angle using a Kruss drop shape analyzer DS-100 instrument. In brief, 2.0 μL water droplets were placed on dried membrane samples using the sessile droplet technique. The water contact angle was calculated between the membrane surface beneath the water droplet and the tangent at the periphery of the water droplet where it meets the membrane surface. The contact angle was measured at five different locations of each membrane to obtain a precise value.

4.5.3. Water Uptake Strength and Porosity Analysis. All the prepared membranes were cut in to five pieces of 2 cm^2 size and plunged in DI water for 24 h. Wet weight of the membranes were noted after withdrawing it from water. To record the dry weight, membrane samples were kept in a vacuum oven at 60 °C for 24 h. A mean of five discrete samples was taken for meticulous calculation. The water intake strength of the membrane was determined using the following equation.

https://doi.org/10.1021/acsomega.3c10078
ACS Omega 2024, 9, 25766−25778

$$\%\ \text{Water uptake} = \left(\frac{W_m - W_d}{W_m}\right) \times 100 \quad (1)$$

where "W_m" and "W_d" represent the moist weight and dried weight of the membrane samples.

To determine the porosity percentage, the following equation was utilized

$$\in(\%) = \left(\frac{W_m - W_d}{Al\rho}\right) \times 100 \quad (2)$$

where "ρ" is the pure water density (0.998 g cm^{-3}), "l" is the membrane thickness (cm), and "A" is the membrane thickness (cm).

4.5.4. Thermal Stability Analysis. The thermal stability and decomposition of VPM-2 membrane was studied in the temperature span of 25−900 °C employing TGA (4000, Perkin-Elmer). A dried membrane sample was used for analysis, and the sample was heated at the pace of 10 °C min^{-1}.

4.5.5. Molecular Weight Cutoff Analysis. The solute of lowest molecular weight showing a rejection above 90% for a membrane is termed as MWCO. It gives an idea of the retention capability and pore size distribution of the membrane. Polyethylene glycol (PEG) of different molecular masses such as 2000, 4000, 6000, and 10,000 Da were filtered through the VPM-2 membrane to determine the MWCO. Filtration was performed with 100 ppm of PEG solution at a 2 bar pressure. The solute concentration in the permeate was calculated using a TOC-L SHIMADZU total organic carbon (TOC) analyzer with regard to TOC. The rejection percentages of PEG solutions were obtained utilizing the following equation.

$$\text{Rejection}\ \% = \left(1 - \frac{C_p}{C_f}\right) \times 100 \quad (3)$$

where C_f and C_p are the solute concentrations of feed and permeate, respectively.

4.5.6. Permeation and Antifouling Study. Water permeability and antifouling studies were carried out using a lab-scale cross-flow filtration setup. Circular membrane with an effective surface area of 23.76 cm^2 was utilized for filtration. In the beginning, the membranes were put through compaction for 30 min at a pressure of 3 bar and then PWF "J_{f1}" was calculated at a pressure of 2 bar for 100 min utilizing the next equation.

$$J_{f_1} = \frac{Q_f}{A\Delta t} \quad (4)$$

where Q_f is the flux obtained in liters, A is the active membrane area, and Δt is the time taken in hours.

In the antifouling study, the membranes were subjected to 30 min compaction at a 3 bar pressure before checking the PWF at 2 bar for 100 min. Then, 800 ppm BSA solution was filtered through the membranes at 2 bar for 100 min. BSA was used as model protein foulant and permeate obtained was noted as "J_b". After BSA filtration, distilled water wash was given to membranes for 5 min and water permeability of washed membranes was calculated as "J_{f_2}" for 100 min. The antifouling nature of the membranes were calculated in terms of FRR, total fouling ratio (R_t), reversible fouling ratio (R_r), and irreversible fouling ratio (R_{ir}) using the following equations.

$$\text{FRR}\ (\%) = \left(\frac{J_{f_2}}{J_{f_1}}\right) \times 100 \quad (5)$$

$$R_r\ (\%) = \left(\frac{J_{f_2} - J_b}{J_{f_1}}\right) \times 100 \quad (6)$$

$$R_{ir}\ (\%) = \left(\frac{J_{f_1} - J_{f_2}}{J_{f_1}}\right) \times 100 \quad (7)$$

$$R_t\ (\%) = \left(\frac{J_{f_1} - J_b}{J_{f_1}}\right) \times 100 \quad (8)$$

where "J_{f_1}", "J_b", and "J_{f_2}" were noted in terms of L m^{-2} h^{-1} bar^{-1}.

4.5.7. Temperature Resistance Study. The temperature resistance and decomposition of VPM-2 membrane was studied in the temperature span of 25−900 °C utilizing TGA (4000, Perkin-Elmer). A dried membrane sample was used for analysis, and the sample was heated at a speed of 10 °C min^{-1}.

4.5.8. Rejection Study. Two dyes, specifically Reactive Orange 16 and Reactive Black 5 were used for rejection study. One more model pollutant, HA, was also used for rejection investigation. All of the solutions were made at a concentration of 100 ppm and filtered through neat PPSU and VPM-2 membranes at a 2 bar pressure. The solute concentration in the feed (C_f) and permeate (C_p) were determined employing an Analytik Jena SPECORD S 600 UV V-Visible spectrometer. The percentage rejection of both the dyes and HA was calculated using the following formula.

$$\text{Percentage of rejection} = \left(1 - \frac{C_p}{C_f}\right) \times 100 \quad (9)$$

■ ASSOCIATED CONTENT

Supporting Information

The Supporting Information is available free of charge at https://pubs.acs.org/doi/10.1021/acsomega.3c10078.

Additional experimental details and methods, including photographs of the experimental setup (PDF)

■ AUTHOR INFORMATION

Corresponding Author

Arun M. Isloor − *Membrane and Separation Technology Laboratory, Department of Chemistry, National Institute of Technology Karnataka, 575 025 Mangalore, India;* orcid.org/0000-0003-2038-3494; Email: isloor@yahoo.com

Authors

Prabhakar Satishkumar − *Membrane and Separation Technology Laboratory, Department of Chemistry, National Institute of Technology Karnataka, 575 025 Mangalore, India*

Lakshmi Nidhi Rao − *Department of Conservative Dentistry and Endodontics, A.B. Shetty Memorial Institute of Dental Sciences, Nitte deemed to be University, 575018 Mangalore, India*

https://doi.org/10.1021/acsomega.3c10078
ACS Omega 2024, 9, 25766−25778

Ramin Farnood − *Department of Chemical Engineering and Applied Chemistry, University of Toronto, M5R OA3 Toronto, Canada;* orcid.org/0000-0002-2680-0036

Complete contact information is available at: https://pubs.acs.org/10.1021/acsomega.3c10078

Funding

Necessary funding for this research was provided by National Institute of Technology Karnataka, Surathkal, India.

Notes

The authors declare no competing financial interest.

■ ACKNOWLEDGMENTS

The authors are thankful to the Director of the National Institute of Technology Karnataka, Surathkal, India, for providing the research facilities. The authors acknowledge CRF, NITK Surathkal for providing analytical facility such as SEM, EDX, AFM, TGA, zeta potential, and particle size analyzer for this research work. Authors also thank Department of Chemical Engineering NITK Surathkal for assisting in analytical studies.

■ REFERENCES

(1) Satishkumar, P.; Isloor, A. M.; Farnood, R. Continuous Production of Clean Hydrogen from Wastewater by Microbial Usage. *Materials for Hydrogen Production, Conversion, and Storage*; John Wiley & Sons, Ltd, 2023; pp 277−318.

(2) Hebbar, R. S.; Isloor, A. M.; Inamuddin; Abdullah, M. S.; Ismail, A. F.; Asiri, A. M. Fabrication of Polyetherimide Nanocomposite Membrane with Amine Functionalised Halloysite Nanotubes for Effective Removal of Cationic Dye Effluents. *J. Taiwan Inst. Chem. Eng.* **2018**, *93*, 42−53.

(3) Ikram, M.; Raza, A.; Imran, M.; Ul-Hamid, A.; Shahbaz, A.; Ali, S. Hydrothermal Synthesis of Silver Decorated Reduced Graphene Oxide (rGO) Nanoflakes with Effective Photocatalytic Activity for Wastewater Treatment. *Nanoscale Res. Lett.* **2020**, *15* (1), 95.

(4) Elbakry, S.; Ali, M. E. A.; Abouelfadl, M.; Badway, N. A.; Salam, K. M. M. Photocatalytic Degradation of Organic Compounds by TFC Membranes Functionalized with Ag/rGO Nanocomposites. *J. Photochem. Photobiol., A* **2022**, *430*, 113957.

(5) Ryu, J.; Jung, J.; Park, K.; Song, W.; Choi, B.; Kweon, J. Humic Acid Removal and Microbial Community Function in Membrane Bioreactor. *J. Hazard. Mater.* **2021**, *417*, 126088.

(6) Panchami, H. R.; Isloor, A. M.; Ismail, A. F. Improved Hydrophilic and Antifouling Performance of Nanocomposite Ultrafiltration Zwitterionic Polyphenylsulfone Membrane for Protein Rejection Applications. *J. Nanostruct. Chem.* **2022**, *12*, 343−364.

(7) Satishkumar, P.; Isloor, A. M.; Farnood, R. Nanocomposite Membranes for Proton Exchange Membrane Fuel Cells. *Proton Exchange Membrane Fuel Cells*; John Wiley & Sons, Ltd, 2023; pp 73−110.

(8) Ng, L. Y.; Mohammad, A. W.; Leo, C. P.; Hilal, N. Polymeric Membranes Incorporated with Metal/Metal Oxide Nanoparticles: A Comprehensive Review. *Desalination* **2013**, *308*, 15−33.

(9) Kumar, R.; Isloor, A. M.; Ismail, A. F.; Rashid, S. A.; Ahmed, A. A. Permeation, Antifouling and Desalination Performance of TiO2 Nanotube Incorporated PSf/CS Blend Membranes. *Desalination* **2013**, *316*, 76−84.

(10) Nair, A. K.; Isloor, A. M.; Kumar, R.; Ismail, A. F. Antifouling and Performance Enhancement of Polysulfone Ultrafiltration Membranes Using CaCO3 Nanoparticles. *Desalination* **2013**, *322*, 69−75.

(11) Isloor, A. M.; Nayak, M. C.; Inamuddin; Prabhu, B.; Ismail, N.; Ismail, A. F.; Asiri, A. M. Novel Polyphenylsulfone (PPSU)/Nano Tin Oxide (SnO2) Mixed Matrix Ultrafiltration Hollow Fiber Membranes: Fabrication, Characterization and Toxic Dyes Removal from Aqueous Solutions. *React. Funct. Polym.* **2019**, *139*, 170−180.

(12) Ibrahim, G. P. S.; Isloor, A. M.; Inamuddin; Asiri, A. M.; Farnood, R. Tuning the Surface Properties of Fe3O4 by Zwitterionic Sulfobetaine: Application to Antifouling and Dye Removal Membrane. *Int. J. Environ. Sci. Technol.* **2020**, *17* (9), 4047−4060.

(13) Kumar, M.; Isloor, A. M.; Todeti, S. R.; Ismail, A. F.; Farnood, R. Hydrophilic Nano-Aluminum Oxide Containing Polyphenylsulfone Hollow Fiber Membranes for the Extraction of Arsenic (As-V) from Drinking Water. *J. Water Proc. Eng.* **2021**, *44*, 102357.

(14) Ganesh, B. M.; Isloor, A. M.; Ismail, A. F. Enhanced Hydrophilicity and Salt Rejection Study of Graphene Oxide-Polysulfone Mixed Matrix Membrane. *Desalination* **2013**, *313*, 199−207.

(15) Han, R.; Ma, X.; Xie, Y.; Teng, D.; Zhang, S. Preparation of a New 2D MXene/PES Composite Membrane with Excellent Hydrophilicity and High Flux. *RSC Adv.* **2017**, *7* (89), 56204−56210.

(16) Liu, G.; Shen, J.; Liu, Q.; Liu, G.; Xiong, J.; Yang, J.; Jin, W. Ultrathin Two-Dimensional MXene Membrane for Pervaporation Desalination. *J. Membr. Sci.* **2018**, *548*, 548−558.

(17) Naguib, M.; Kurtoglu, M.; Presser, V.; Lu, J.; Niu, J.; Heon, M.; Hultman, L.; Gogotsi, Y.; Barsoum, M. W. Two-Dimensional Nanocrystals Produced by Exfoliation of Ti3AlC2. *Adv. Mater.* **2011**, *23* (37), 4248−4253.

(18) Kannan, K.; Sadasivuni, K. K.; Abdullah, A. M.; Kumar, B. Current Trends in MXene-Based Nanomaterials for Energy Storage and Conversion System: A Mini Review. *Catalysts* **2020**, *10* (5), 495.

(19) Pei, Y.; Zhang, X.; Hui, Z.; Zhou, J.; Huang, X.; Sun, G.; Huang, W. Ti3C2TX MXene for Sensing Applications: Recent Progress, Design Principles, and Future Perspectives. *ACS Nano* **2021**, *15* (3), 3996−4017.

(20) Morales-García, Á.; Calle-Vallejo, F.; Illas, F. MXenes: New Horizons in Catalysis. *ACS Catal.* **2020**, *10* (22), 13487−13503.

(21) Jun, B.-M.; Her, N.; Park, C. M.; Yoon, Y. Effective Removal of Pb(II) from Synthetic Wastewater Using Ti3C2Tx MXene. *Environ. Sci.: Water Res. Technol.* **2020**, *6* (1), 173−180.

(22) Meng, F.; Seredych, M.; Chen, C.; Gura, V.; Mikhalovsky, S.; Sandeman, S.; Ingavle, G.; Ozulumba, T.; Miao, L.; Anasori, B.; Gogotsi, Y. MXene Sorbents for Removal of Urea from Dialysate: A Step toward the Wearable Artificial Kidney. *ACS Nano* **2018**, *12* (10), 10518−10528.

(23) Karahan, H. E.; Goh, K.; Zhang, C. J.; Yang, E.; Yıldırım, C.; Chuah, C. Y.; Ahunbay, M. G.; Lee, J.; Tantekin-Ersolmaz, Ş. B.; Chen, Y.; Bae, T.-H. MXene Materials for Designing Advanced Separation Membranes. *Adv. Mater.* **2020**, *32* (29), 1906697.

(24) Ding, L.; Wei, Y.; Wang, Y.; Chen, H.; Caro, J.; Wang, H. A Two-Dimensional Lamellar Membrane: MXene Nanosheet Stacks. *Angew. Chem., Int. Ed.* **2017**, *56* (7), 1825−1829.

(25) Lin, Q.; Liu, Y.; Zeng, G.; Li, X.; Wang, B.; Cheng, X.; Sengupta, A.; Yang, X.; Feng, Z. Bionics Inspired Modified Two-Dimensional MXene Composite Membrane for High-Throughput Dye Separation. *J. Environ. Chem. Eng.* **2021**, *9* (4), 105711.

(26) Zhang, L.; Liu, Y.; Zeng, G.; Yang, Z.; Lin, Q.; Wang, Y.; Wang, X.; Pu, S. Two-Dimensional Na-Bentonite@MXene Composite Membrane with Switchable Wettability for Selective Oil/Water Separation. *Sep. Purif. Technol.* **2023**, *306*, 122677.

(27) Zhang, H.; Zheng, Y.; Zhou, H.; Zhu, S.; Yang, J. Nanocellulose-Intercalated MXene NF Membrane with Enhanced Swelling Resistance for Highly Efficient Antibiotics Separation. *Sep. Purif. Technol.* **2023**, *305*, 122425.

(28) Wang, Q.; Yu, Z.; Zhu, X.; Xiang, Q.; Chen, H.; Pang, Y. ZIF-67 Modified MXene/Sepiolite Composite Membrane for Oil-Water Separation and Heavy Metal Removal. *J. Ind. Eng. Chem.* **2022**, *115*, 314−328.

(29) Azam, R. S.; Almasri, D. A.; Alfahel, R.; Hawari, A. H.; Hassan, M. K.; Elzatahry, A. A.; Mahmoud, K. A. MXene (Ti3C2Tx)/Cellulose Acetate Mixed-Matrix Membrane Enhances Fouling Resistance and Rejection in the Crossflow Filtration Process. *Membranes* **2022**, *12* (4), 406.

(30) Dashtbozorg, A.; Saljoughi, E.; Mousavi, S. M.; Kiani, S. High-Performance and Robust Polysulfone Nanocomposite Membrane Containing 2D Functionalized MXene Nanosheets for the Nanofiltration of Salt and Dye Solutions. *Desalination* **2022**, *527*, 115600.
(31) Matthews, K.; Zhang, T.; Shuck, C. E.; VahidMohammadi, A.; Gogotsi, Y. Guidelines for Synthesis and Processing of Chemically Stable Two-Dimensional V_2CT_x MXene. *Chem. Mater.* **2022**, *34* (2), 499−509.
(32) VahidMohammadi, A.; Mojtabavi, M.; Caffrey, N. M.; Wanunu, M.; Beidaghi, M. Assembling 2D MXenes into Highly Stable Pseudocapacitive Electrodes with High Power and Energy Densities. *Adv. Mater.* **2019**, *31* (8), 1806931.
(33) Huang, D.; Xie, Y.; Lu, D.; Wang, Z.; Wang, J.; Yu, H.; Zhang, H. Demonstration of a White Laser with V2C MXene-Based Quantum Dots. *Adv. Mater.* **2019**, *31* (24), 1901117.
(34) VahidMohammadi, A.; Hadjikhani, A.; Shahbazmohamadi, S.; Beidaghi, M. Two-Dimensional Vanadium Carbide (MXene) as a High-Capacity Cathode Material for Rechargeable Aluminum Batteries. *ACS Nano* **2017**, *11* (11), 11135−11144.
(35) Lee, E.; VahidMohammadi, A.; Yoon, Y. S.; Beidaghi, M.; Kim, D.-J. Two-Dimensional Vanadium Carbide MXene for Gas Sensors with Ultrahigh Sensitivity Toward Nonpolar Gases. *ACS Sens.* **2019**, *4* (6), 1603−1611.
(36) Wang, L.; Yuan, L.; Chen, K.; Zhang, Y.; Deng, Q.; Du, S.; Huang, Q.; Zheng, L.; Zhang, J.; Chai, Z.; Barsoum, M. W.; Wang, X.; Shi, W. Loading Actinides in Multilayered Structures for Nuclear Waste Treatment: The First Case Study of Uranium Capture with Vanadium Carbide MXene. *ACS Appl. Mater. Interfaces* **2016**, *8* (25), 16396−16403.
(37) Liu, F.; Zhou, J.; Wang, S.; Wang, B.; Shen, C.; Wang, L.; Hu, Q.; Huang, Q.; Zhou, A. Preparation of High-Purity V2C MXene and Electrochemical Properties as Li-Ion Batteries. *J. Electrochem. Soc.* **2017**, *164* (4), A709−A713.
(38) Ling, C.; Shi, L.; Ouyang, Y.; Chen, Q.; Wang, J. Transition Metal-Promoted V2CO2 (MXenes): A New and Highly Active Catalyst for Hydrogen Evolution Reaction. *Advanced Science* **2016**, *3* (11), 1600180.
(39) Wang, L.; Liu, D.; Lian, W.; Hu, Q.; Liu, X.; Zhou, A. The Preparation of V2CTx by Facile Hydrothermal-Assisted Etching Processing and Its Performance in Lithium-Ion Battery. *J. Mater. Res. Technol.* **2020**, *9* (1), 984−993.
(40) Li, Y.; Zhou, X.; Wang, J.; Deng, Q.; Li, M.; Du, S.; Han, Y.-H.; Lee, J.; Huang, Q. Facile Preparation of in Situ Coated Ti3C2Tx/Ni0.5Zn0.5Fe2O4 Composites and Their Electromagnetic Performance. *RSC Adv.* **2017**, *7* (40), 24698−24708.
(41) Slaouti, H.; Boutamine, S.; Hank, Z.; Zekri, O.; Meklati, M.; Vittori, O. Synthesis and Characterisation of Some Vanadium(V) and (IV) Compounds with Benzaldoxime. *Synth. React. Inorg. Met.-Org. Chem.* **2004**, *34* (10), 1801−1815.
(42) O'Dwyer, C.; Lavayen, V.; Newcomb, S. B.; Santa Ana, M. A.; Benavente, E.; González, G.; Sotomayor Torres, C. M. Vanadate Conformation Variations in Vanadium Pentoxide Nanostructures. *J. Electrochem. Soc.* **2007**, *154* (8), K29.
(43) Rasool, K.; Helal, M.; Ali, A.; Ren, C. E.; Gogotsi, Y.; Mahmoud, K. A. Antibacterial Activity of $Ti_3C_2T_x$ MXene. *ACS Nano* **2016**, *10* (3), 3674−3684.
(44) Naguib, M.; Halim, J.; Lu, J.; Cook, K. M.; Hultman, L.; Gogotsi, Y.; Barsoum, M. W. New Two-Dimensional Niobium and Vanadium Carbides as Promising Materials for Li-Ion Batteries. *J. Am. Chem. Soc.* **2013**, *135* (43), 15966−15969.
(45) Chen, K.; Zhang, T.; Chen, X.; He, Y.; Liang, X. Model Construction of Micro-Pores in Shale: A Case Study of Silurian Longmaxi Formation Shale in Dianqianbei Area, SW China. *Pet. Explor. Dev.* **2018**, *45* (3), 412−421.
(46) Günister, E.; İşçi, S.; Öztekin, N.; Erim, F. B.; Ece, Ö. I.; Güngör, N. Effect of Cationic Surfactant Adsorption on the Rheological and Surface Properties of Bentonite Dispersions. *J. Colloid Interface Sci.* **2006**, *303* (1), 137−141.
(47) Ibrahim, G. S.; Isloor, A. M.; Inamuddin; Asiri, A. M.; Ismail, A. F.; Kumar, R.; Ahamed, M. I. Performance Intensification of the Polysulfone Ultrafiltration Membrane by Blending with Copolymer Encompassing Novel Derivative of Poly(Styrene-Co-Maleic Anhydride) for Heavy Metal Removal from Wastewater. *Chem. Eng. J.* **2018**, *353*, 425−435.
(48) Liu, Y.; Yue, X.; Zhang, S.; Ren, J.; Yang, L.; Wang, Q.; Wang, G. Synthesis of Sulfonated Polyphenylsulfone as Candidates for Antifouling Ultrafiltration Membrane. *Sep. Purif. Technol.* **2012**, *98*, 298−307.
(49) Jiang, J.-H.; Zhu, L.-P.; Zhang, H.-T.; Zhu, B.-K.; Xu, Y.-Y. Improved Hydrodynamic Permeability and Antifouling Properties of Poly(Vinylidene Fluoride) Membranes Using Polydopamine Nanoparticles as Additives. *J. Membr. Sci.* **2014**, *457*, 73−81.
(50) Hebbar, R. S.; Isloor, A. M.; Ananda, K.; Ismail, A. F. Fabrication of Polydopamine Functionalized Halloysite Nanotube/Polyetherimide Membranes for Heavy Metal Removal. *J. Mater. Chem. A* **2016**, *4* (3), 764−774.
(51) Mi, F.-L.; Wu, Y.-B.; Shyu, S.-S.; Chao, A.-C.; Lai, J.-Y.; Su, C.-C. Asymmetric Chitosan Membranes Prepared by Dry/Wet Phase Separation: A New Type of Wound Dressing for Controlled Antibacterial Release. *J. Membr. Sci.* **2003**, *212* (1−2), 237−254.
(52) Qu, P.; Tang, H.; Gao, Y.; Zhang, L.; Wang, S. Polyethersulfone Composite Membrane Blended With Cellulose Fibrils. *Bioresources* **2010**, *5*, 2323−2336.
(53) Zhao, P.; Gao, B.; Yue, Q.; Shon, H. K.; Li, Q. Fouling of Forward Osmosis Membrane by Protein (BSA): Effects of pH, Calcium, Ionic Strength, Initial Permeate Flux, Membrane Orientation and Foulant Composition. *Desalin. Water Treat.* **2016**, *57* (29), 13415−13424.
(54) Matthiasson, E.; Sivik, B. Concentration Polarization and Fouling. *Desalination* **1980**, *35*, 59−103.
(55) One-step synthesis and characterization of hydrophilic polymer microspheresimmobilized with polyphenylsulfone ultrafiltration membranes for protein rejection application. **2022**..
(56) Zinadini, S.; Zinatizadeh, A. A.; Rahimi, M.; Vatanpour, V.; Zangeneh, H. Preparation of a Novel Antifouling Mixed Matrix PES Membrane by Embedding Graphene Oxide Nanoplates. *J. Membr. Sci.* **2014**, *453*, 292−301.
(57) Chen, S.; Li, L.; Zhao, C.; Zheng, J. Surface Hydration: Principles and Applications toward Low-Fouling/Nonfouling Biomaterials. *Polymer* **2010**, *51* (23), 5283−5293.
(58) Hebbar, R. S.; Isloor, A. M.; Prabhu, B.; Inamuddin; Asiri, A. M.; Ismail, A. F. Removal of Metal Ions and Humic Acids through Polyetherimide Membrane with Grafted Bentonite Clay. *Sci. Rep.* **2018**, *8* (1), 4665.
(59) Shao, J.; Hou, J.; Song, H. Comparison of Humic Acid Rejection and Flux Decline during Filtration with Negatively Charged and Uncharged Ultrafiltration Membranes. *Water Res.* **2011**, *45* (2), 473−482.
(60) Ibrahim, G. P. S.; Isloor, A. M.; Inamuddin; Asiri, A. M.; Ismail, N.; Ismail, A. F.; Ashraf, G. M. Novel, One-Step Synthesis of Zwitterionic Polymer Nanoparticles via Distillation-Precipitation Polymerization and Its Application for Dye Removal Membrane. *Sci. Rep.* **2017**, *7* (1), 15889.
(61) Nayak, M. C.; Isloor, A. M.; Moslehyani, A.; Ismail, N.; Ismail, A. F. Fabrication of Novel PPSU/ZSM-5 Ultrafiltration Hollow Fiber Membranes for Separation of Proteins and Hazardous Reactive Dyes. *J. Taiwan Inst. Chem. Eng.* **2018**, *82*, 342−350.
(62) Pandey, R. P.; Rasool, K.; Madhavan, V. E.; Aïssa, B.; Gogotsi, Y.; Mahmoud, K. A. Ultrahigh-Flux and Fouling-Resistant Membranes Based on Layered Silver/MXene (Ti3C2Tx) Nanosheets. *J. Mater. Chem. A* **2018**, *6* (8), 3522−3533.
(63) Feng, X.; Yu, Z.; Long, R.; Sun, Y.; Wang, M.; Li, X.; Zeng, G. Polydopamine Intimate Contacted Two-Dimensional/Two-Dimensional Ultrathin Nylon Basement Membrane Supported RGO/PDA/MXene Composite Material for Oil-Water Separation and Dye Removal. *Sep. Purif. Technol.* **2020**, *247*, 116945.

https://doi.org/10.1021/acsomega.3c10078
ACS Omega 2024, 9, 25766−25778

(64) Yao, Y.; Wang, T.; Wu, L.; Chen, H. PES Mixed-Matrix Membranes Incorporating ZIF-8@MXene Nanocomposite for the Efficient Dye/Salt Separation. *Desalination* **2022**, *543*, 116116.
(65) Li, J.; Li, L.; Xu, Y.; Zhu, J.; Liu, F.; Shen, J.; Wang, Z.; Lin, J. MXene Nanosheet Stacks with Tunable Nanochannels for Efficient Molecular Separation. *Chem. Eng. J.* **2022**, *427*, 132070.
(66) Alhabeb, M.; Maleski, K.; Anasori, B.; Lelyukh, P.; Clark, L.; Sin, S.; Gogotsi, Y. Guidelines for Synthesis and Processing of Two-Dimensional Titanium Carbide ($Ti_3C_2T_x$ MXene). *Chem. Mater.* **2017**, *29* (18), 7633−7644.

https://doi.org/10.1021/acsomega.3c10078
ACS Omega 2024, 9, 25766−25778